

AN INSTRUMENT FOR INVESTIGATING THE LARGE ANGULAR SCALE POLARIZATION OF THE COSMIC MICROWAVE BACKGROUND

BRIAN G. KEATING¹, CHRISTOPHER W. O'DELL, JOSHUA O. GUNDERSEN², LUCIO PICCIRILLO³,
NATE C. STEBOR⁴, AND PETER T. TIMBIE

Department of Physics, 2531 Sterling Hall, University of Wisconsin – Madison, Madison, WI 53706

Draft version October 23, 2018

ABSTRACT

We describe the design and performance of a microwave polarimeter used to make precision measurements of polarized astrophysical radiation in three microwave frequency bands spanning 26-36 GHz. The instrument uses cooled HEMT amplifiers in a correlation polarimeter configuration to achieve high sensitivity and long-term stability. The instrument demonstrates long term stability and has produced the most restrictive upper limits to date on the large angular scale polarization of the 2.7 K cosmic microwave background radiation.

Subject headings: cosmic microwave background: – cosmology: observations, instrumentation, polarimeters

1. INTRODUCTION

Observations of the cosmic microwave background (CMB) are some of the most powerful tools in cosmology. The CMB has the promise to address the most fundamental cosmological questions: the geometry and age of the universe, the matter content of the universe, the ionization history and the spectrum of primordial perturbations. The CMB is specified by three characteristics: its spectrum, the spatial distribution of its total intensity, and the spatial distribution of its polarization. All three properties depend on the fundamental cosmological parameters. Several instruments have produced precision measurements of its spectrum and anisotropy at large, medium, and small angular scales (see, for example, Wang, Tegmark, & Zaldarriaga 2001) and references therein).

Similar to the CMB anisotropy power spectrum, the polarization power spectrum encodes information on all angular scales. Large angular scales ($> 1^\circ$) correspond to regions on the last scattering surface which were larger than the causal horizon at that time. In the absence of reionization, polarization on these scales was affected only by the longest wavelength modes of the primordial power spectrum. Reionization is expected to produce a new polarized peak in the power spectrum near $\ell \lesssim 20$, where the precise peak location depends on the redshift at which the Universe (Zaldarriaga 1998; Keating et al. 1998) became reionized.

The large scale region of the anisotropy power spectrum was measured by the *COBE* DMR, and this established the normalization for models of large scale structure formation. The effect of reionization on the anisotropy power spectrum is to damp all angular scales by a factor of $e^{-2\tau}$ where τ is the optical depth to the reionization epoch. This effect is degenerate with several other cosmological

parameters (Zaldarriaga 1997) and non-zero τ cannot be unambiguously detected, at any scale, from the anisotropy power spectrum alone. Similarly, the effect of gravitational waves on the anisotropy power spectrum is also degenerate with other cosmological parameters (Zaldarriaga, Spergel, & Seljak 1997). Detection of CMB polarization at scales $> 1^\circ$ has the potential to detect reionization and primordial gravitational waves.

Although the polarization signal at large angular scales is expected to be weaker than at small scales, the design of a large angular scale experiment is simpler and more compact than an experiment probing small scales. A large angular scale experiment with no external beam forming optics (*i.e.*, no primary mirror), exhibits minimal spurious polarization and reduces susceptibility to numerous sources of systematic error. In this paper we describe our approach to measuring the large scale polarization of the CMB: Polarization Observations of Large Angular Regions (POLAR).

POLAR's design builds on techniques developed in previous searches for CMB polarization (Nanos 1979; Lubin & Smoot 1981; Wollack et al. 1997) and is driven by the size and angular scale of the anticipated CMB signals, spectral removal of foreground sources, optimization of the observing scheme, long-term stability, and immunity to potential systematic effects. POLAR is a wide bandwidth (~ 8 GHz) correlation polarimeter dedicated to measurements of the CMB. POLAR measures polarization in the K_a band, between 26 and 36 GHz, using cooled High Electron Mobility Transistor (HEMT) amplifiers. This band is multiplexed into three sub-bands to allow for discrimination against foreground sources. The radiometer executes a zenith drift scan with a 7° FWHM beam produced by a corrugated feed horn antenna. In the Spring of 2000 POLAR observed a $\simeq 7^\circ$ wide region from $RA = 112^\circ$ to 275° at declination 43° for 45 days from the University of Wisconsin – Madison's Pine Bluff Observatory in Pine Bluff, Wisconsin (Latitude $+43^\circ 01'$, Longitude $+89^\circ 45'$). In a single night of data POLAR achieved a sensitivity level of $\sim 50 \mu\text{K}$ to the Stokes parameters Q and U in each beam-sized pixel. For the 2000 season POLAR set upper limits on the amplitude of the cosmological E-mode and B-mode (Zaldarriaga & Seljak 1997; Kamionkowski, Kosowsky, &

¹ Current Address: Division of Physics, Math, and Astronomy, California Institute of Technology, Pasadena, CA 91125; bgk@astro.caltech.edu.

² Department of Physics, University of Miami, Coral Gables, FL 33146

³ Department of Physics and Astronomy, University of Wales - Cardiff, Wales, UK CF24 3YB

⁴ Department of Physics, University of California at Santa Barbara, Santa Barbara, CA 93106

Stebbins 1997) power spectra of $T_E, T_B < 10 \mu\text{K}$ at 95% confidence (Keating et al. 2001).

In this paper we describe the design and performance of POLAR. In section 2 we outline the fundamentals of the correlation polarimeter. Section 3 presents detailed instrument design specifications and performance. Section 4 describes our calibration technique, and section 5 addresses potential systematic effects and radiometric offset characterization. Finally, section 6 summarizes the meteorological conditions encountered during the observation run as well as our data selection criteria.

2. CORRELATION POLARIMETER

The correlation polarimeter is based on a correlation radiometer (Fujimoto 1964; Rohlfs 1996), which shares many technological features with an interferometer Thompson et al. (1998). The development of the correlation radiometer preceded the discovery of the CMB in 1965; see for example Fujimoto (1964). Several early CMB experiments used correlation radiometers for anisotropy measurements (Cheng et al. 1979), spectral measurements (Johnson & Wilkinson 1987), and the first application of a dedicated interferometer to CMB research (Timbie & Wilkinson 1990).

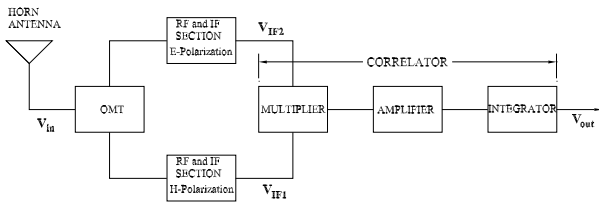


FIG. 1.— Schematic of a simple correlation polarimeter. Radio-frequency fields are split into two linear polarization states by an orthomode transducer (OMT), and amplified. The rectangular waveguide output ports of the OMT define the perpendicular E and H planes of the polarimeter. The field amplitudes are multiplied, producing a DC voltage proportional to their product. The DC product voltage is filtered and amplified before being integrated (low-pass filtered) prior to being recorded.

In a correlation polarimeter the two linear polarization components of an incident electric field are separated and processed in two discrete radiometer chains. For an electric field propagating in the $\hat{\mathbf{z}}$ direction, at an electromagnetic frequency ν , $\mathbf{E}(\nu, t) = E_x(t) \cos(2\pi\nu t + \phi_x) \hat{\mathbf{x}} + E_y(t) \cos(2\pi\nu t + \phi_y) \hat{\mathbf{y}}$, the Stokes parameters are defined by:

$$I \equiv E_x^2(t) + E_y^2(t) \quad (1)$$

$$Q \equiv E_x^2(t) - E_y^2(t) \quad (2)$$

$$U \equiv \langle 2E_y(t)E_x(t) \cos(\phi_x - \phi_y) \rangle \quad (3)$$

$$V \equiv \langle 2E_y(t)E_x(t) \sin(\phi_x - \phi_y) \rangle \quad (4)$$

where the angular brackets denote the expectation value or time-average. For completely linearly polarized radiation, $U = \langle 2E_y(t)E_x(t) \rangle$ and $V = 0$. A simplified correlation polarimeter is shown in figure 1. In a correlation polarimeter the incident field collected by the feedhorn is decomposed into two orthogonal polarization spatial modes,

defined by the rectangular waveguide axes of the polarization diplexer (orthogonal mode transducer – OMT). The fields, now properly described as voltages, are amplified in separate amplifier chains and the output voltages are multiplied and averaged, resulting in a signal proportional to the U Stokes parameter (equation 3). As the polarimeter is rotated about the $\hat{\mathbf{z}}$ axis by an angle θ the correlator output varies as $R(\theta) \propto U \cos 2\theta + Q \sin 2\theta$.

Physically, the correlator (multiplier) is based on a diode bridge which acts as a mixer when provided with an AC bias waveform. The uncorrelated RF power in each arm provides the bias power for the diodes. An advantage of this detection mechanism is that probes the RF fields at frequencies much higher than the $1/f$ knee of the RF amplifiers. It requires no moving parts which complicate CMB experiments that spatially modulate the incoming signals to overcome low frequency drifts. A variation of the correlation polarimeter design correlates left and right circular polarization modes, and is able to recover all four Stokes parameters simultaneously⁵ (Sironi et al. 1997; Carretti et al. 2001).

The electric field entering the feedhorn at time t , in polarization state $i \in \{x, y\}$ from a source in direction θ (with respect to the feed boresight axis) is expanded into:

$$\tilde{E}_i(\theta, \nu) = \int_{-\infty}^{+\infty} E(\theta, t) e^{-i2\pi\nu t - \phi_i} dt$$

$$E_i(\theta, t) = \int_{-\infty}^{+\infty} \tilde{E}_i(\theta, \nu) e^{i2\pi\nu t + \phi_i} d\nu.$$

The x, y coordinate basis is defined by the orthogonal E and H output waveguide ports of the OMT.

The antenna output voltage for polarization state i is

$$\tilde{V}_i(\nu) = 2\pi \int_{-\pi}^{+\pi} \tilde{E}_i(\theta, \nu) \tilde{G}(\theta, \nu) d\theta, \quad (5)$$

where $\tilde{G}(\theta, \nu)$ is the horn’s (axisymmetric) voltage response function. The output voltage for each polarization, after amplification with total radiometer voltage transfer function $\tilde{H}(\nu)$, is $V'_i(\nu) = \tilde{H}(\nu) \tilde{V}_i(\nu)$. The correlator produces the *complex* correlation function, at time lag τ , of the two voltages:

$$R(\tau) = \lim_{T \rightarrow \infty} \frac{4\pi^2}{2T} \int_{-T}^{+T} V_x(t) V_y^*(t - \tau) dt$$

$$= \lim_{T \rightarrow \infty} \frac{4\pi^2}{2T} \int_{-T}^{+T} dt \int_{-\infty}^{+\infty} d\nu_x \int_{-\infty}^{+\infty} d\nu_y \int_0^\pi d\theta_x \int_0^\pi d\theta_y$$

$$\times \tilde{E}_x(\theta, \nu_x) \tilde{E}_y^*(\theta', \nu_y) \tilde{H}_x(\nu_x) \tilde{H}_y^*(\nu_y) \tilde{G}_x(\theta_x, \nu_x) \tilde{G}_y^*(\theta_y, \nu_y)$$

$$\times e^{i(2\pi\nu_x t + \phi_x)} e^{-i(2\pi\nu_y(t - \tau) + \phi_y)} \quad (6)$$

Remembering that $\int_{-\infty}^{+\infty} e^{2\pi i t(\nu_x - \nu_y)} dt = \delta(\nu_x - \nu_y)$, we obtain:

$$R(\tau) = 4\pi^2 \int_{-T}^{+T} \int_0^\pi \int_0^\pi d\nu d\theta_x d\theta_y$$

$$\times \tilde{\gamma}(\nu, \theta_x, \theta_y) \tilde{B}(\nu, \theta) \tilde{H}_x(\nu) \tilde{H}_y^*(\nu) e^{i(2\pi\nu\tau + \Delta\phi)} \quad (7)$$

⁵ A disadvantage of the circular mode correlation polarimeter is that conversion between Q and U can occur, whereas for linear correlation polarimeters (such as POLAR) primarily conversion between U and V (or Q and V) occurs (Thompson et al. 1998; Carretti et al. 2001). Since $V \ll Q, U$ (either cosmological or systematic), polarization conversion is negligible for POLAR. However, both correlation polarimeter methods suffer from conversion between I and Q and U as discussed below.

where:

$$\tilde{\gamma}(\nu, \theta_x, \theta_y) = \lim_{T \rightarrow \infty} \frac{1}{2T} [\tilde{E}_x(\theta, \nu) \tilde{E}_y^*(\theta', \nu)] \quad (8)$$

is the *source coherence function*, $\Delta\phi = \phi_x - \phi_y$, and

$$\tilde{B}(\nu, \theta_x, \theta_y) = \tilde{G}_x(\theta_x, \nu) \tilde{G}_y^*(\theta_y, \nu).$$

In practice, it is not necessary to enforce $T \rightarrow \infty$, as long as $T \gg 1/\nu$. If, as is the case for POLAR, $\tilde{G}_x(\theta_x, \nu) \simeq \tilde{G}_y(\theta_y, \nu) \equiv \tilde{G}(\theta, \nu)$, then $B(\nu, \theta) = |\tilde{G}(\theta, \nu)|^2$ is the power response function of the horn, or *beam pattern*. For a thermal source, such as the CMB, $\tilde{\gamma}(\nu, \theta, \theta') = \tilde{\gamma}(\nu, \theta) \delta(\theta - \theta')$. For POLAR $\tilde{H}_x(\nu) \simeq \tilde{H}_y(\nu) \equiv \tilde{H}(\nu)$, and only the real part of the complex correlation function is measured with zero lag. Thus, POLAR's output can be expressed as:

$$R_o = 4\pi^2 \int_{-\infty}^{+\infty} d\nu \int_0^{+\pi} d\theta \tilde{\gamma}(\nu, \theta) \tilde{B}(\nu, \theta) |\tilde{H}(\nu)|^2 \cos(\Delta\phi_\nu) \quad (9)$$

where the ν subscript on $\Delta\phi$ incorporates a (potentially) frequency dependent phase shift between the two arms of the radiometer; see section 5.3. The properties of the source coherence function, the transfer functions, and the beam response completely determine the output voltage. Equation 9 will be useful in section 4 where POLAR's response to completely correlated, polarized signals produced by calibration sources is computed.

2.1. Minimum Detectable Signal

The sensitivity of the correlation polarimeter depends on both the system noise temperature and the RF bandwidth of the system. Since there are two RF amplifier chains, the system temperature is their geometric mean: $T_{sys} = \sqrt{T_{sys}^E T_{sys}^H}$, and the minimum detectable signal in an integration time τ is:

$$\Delta T = \sqrt{\frac{2T_{sys}^E T_{sys}^H}{\Delta\nu_{RF} \tau \cos^2 \langle \Delta\phi \rangle_\nu}}, \quad (10)$$

where $\Delta\nu_{RF}$ is the RF bandwidth, and E and H refer to the orthogonal polarization states separated by the OMT (Thompson et al. 1998). Here, we define $\langle \Delta\phi \rangle_\nu$ as the band-averaged differential phase shift between the two arms prior to correlation: $\int_0^\infty \Delta\phi(\nu) d\nu / \int_0^\infty \Delta\phi^2(\nu) d\nu$. Depending on the physical nature of the differential phase shift (e.g., differential guide length, dielectric or microstrip dispersion, etc.) the phase shift may be calculable and/or separable from other sources of bandwidth degradation. In POLAR, all passive waveguide components are matched in length, and adjustable coaxial phase shifters prior to correlation are employed to minimize the contribution of path length phase differences. Equation 10 is valid only when there are no RF gain or offset fluctuations. The effects of radiometer offset, stability, and other non-idealities are discussed in section 5.

3. THE POLAR RADIOMETER

POLAR's radiometer is comprised of three sections: 1) cold receiver components: optics, OMT, isolators, HEMT amplifiers, 2) room-temperature receiver components: warm RF amplifiers, heterodyne stage, warm IF amplifiers, band-defining filters, correlators, and 3) post-detection components: pre-amplifiers, low frequency processing, and data acquisition. In this section the details of the experimental design are presented.

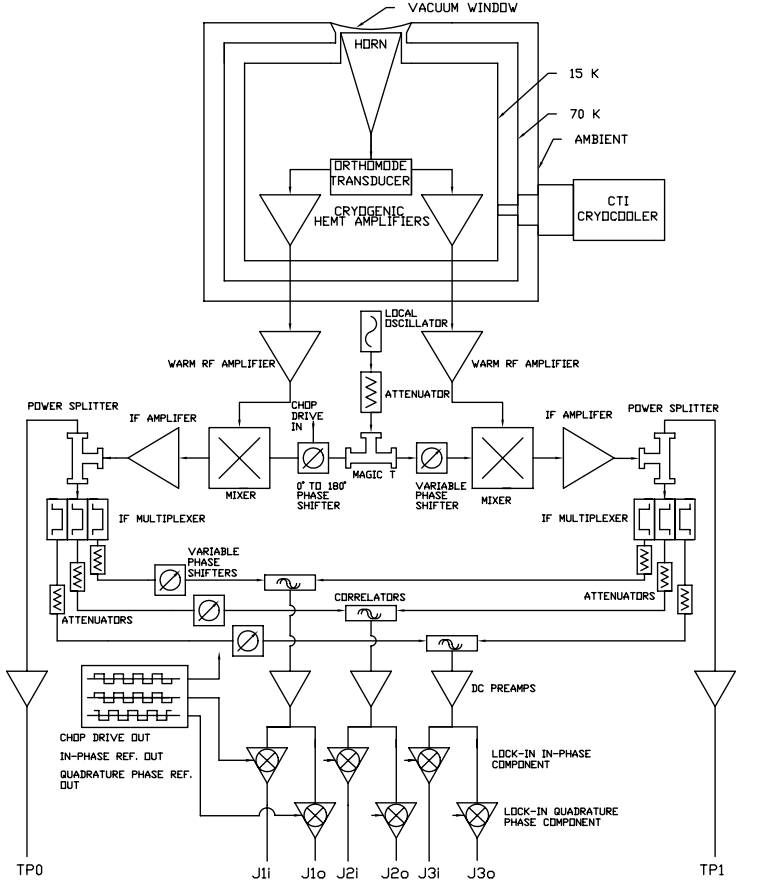


FIG. 2.— Schematic of the POLAR K_a -band correlation polarimeter.

3.1. Cryogenics

The dewar (figure 3) was custom fabricated⁶ to house a cryocooler coldhead, and is large enough to accommodate possible upgrades including additional feed horns in the nominal 20 K (second stage) working volume. The first stage is used to cool a radiation shield, which is maintained at a nominal temperature of ~ 80 K.

Following pump-down to $\sim 1 \times 10^{-4}$ Torr, the pump is detached and the cryocooler's compressor (CTI 8500 Air Cooled) is activated. In the field it was found that the ultimate cold stage temperatures are correlated with the ambient temperature of the shelter in which POLAR resides. The compressor is air-cooled; water cooling was not possible due to the receiver's continuous rotation. The air cooling causes the compressor's compression ratio to be a function of ambient temperature, which modifies its cooling efficiency. Maintaining the temperature stability of the compressor is accomplished, to first order, by a commercial air-conditioner during the summer months which counters the ~ 2 kW heat output from the compressor. During the winter, the heat output by the compressor kept the enclosed POLAR shelter at a nearly constant temperature. The compressor is mechanically isolated from the radiometer by use of a separate rotation bearing coupled loosely to the motor-driven main bearing by copper braid (see figure

⁶ Precision Cryogenic Systems: Indianapolis, IN

7). The compressor is further isolated on its bearing by use of rubber padding on all support structures.

The cold radiometer components are mounted on the 20 K stage, located inside the 80 K stage radiation shield. Both waveguide outputs from the HEMTs connect to vacuum-tight WR-28 stainless steel waveguide feedthroughs⁷ on the 300 K dewar wall. The feedthroughs are mounted on a single flange, which also serves as a feedthrough for the HEMT bias wiring and the temperature diode readout wiring. The final major port in the dewar is the main vacuum optical window. This port is located ~ 3 inches radially off the rotation axis of the cryostat to allow for additional feed horns at higher frequency.

3.2. Optics

POLAR's RF optical system is composed of a single corrugated feed horn. Due to the absence of supplemental beam-forming reflectors, cross-polarization of the instrument is near the minimum possible level for a millimeter wave receiver. POLAR's feed horn design is based on the procedure outlined in Zhang et al. (1993), and is similar to the K_a -band feed horn employed by the *COBE* DMR experiment (Janssen et al. 1979). The horn exhibits symmetry between its E and H planes and produces a diffraction-limited power response with a $\simeq 7^\circ$ full-width-at-half-maximum (FWHM) across the band.

The beam pattern for the POLAR feed was computed using an 11 term Gauss-Laguerre model (Clarricoats & Olver 1984) to predict the far-field beam pattern out to

⁷ Aerowave Corp., Medford, MA

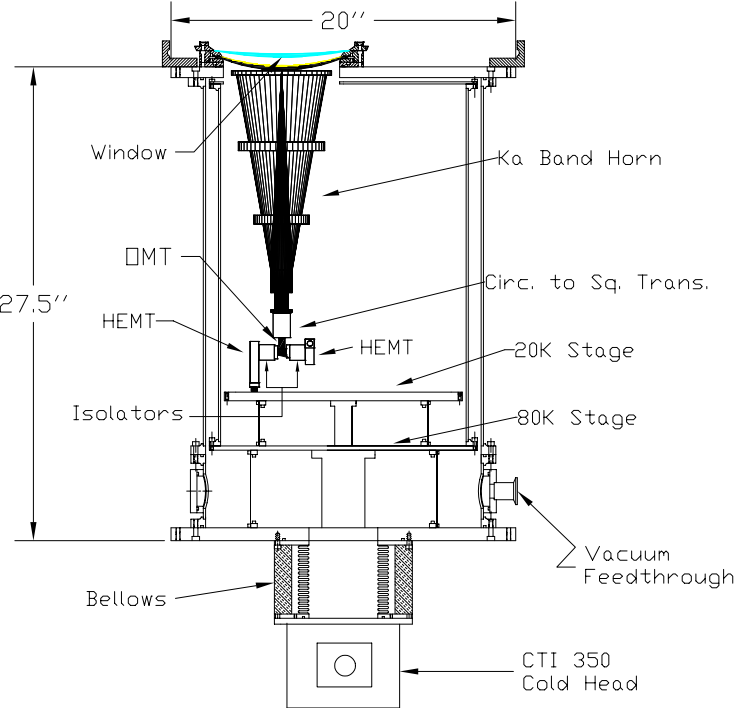


FIG. 3.— POLAR dewar and K_a -band cold receiver components. The horn is located off of the symmetry axis of the dewar in order to allow for future receivers to perform simultaneous observations. The HEMT outputs travel via stainless steel waveguides to a flange on the dewar bottom.

TABLE 1
POLAR INSTRUMENT

Channel ^a	ν_c ^b [GHz]	$\Delta\nu$ ^c [GHz]	Ω_B ^d [$^\circ$]	$\overline{T}_{\text{pol}}$ ^e [μK]	S_{sky} ^f [$\text{mK s}^{1/2}$]	T_{rec} ^g [K]
TP-E/H	31.9	7.8/8.0	7.0	...	14.0/20.0	32
J3	27.5	1.3	7.5	84(28)	2.0	43
J2	30.5	3.1	7.0	72(14)	1.2	34
J1	34.0	3.1	6.4	33(11)	1.1	33

^aTP-E and TP-H measure the total power in the E and H polarization planes of the Horn/OMT assembly prior to correlation.

^bChannel band centroid measured with swept, coherent source.

^cMeasured channel bandwidth.

^dBeamwidths (FWHM). E and H-plane Beamwidths are equal to within 1%. Measured feed/OMT cross-polarization is < -40 dB for all channels.

^eMean polarized offset for the Spring 2000 observing season. $\overline{T}_{\text{pol}} = \sqrt{\overline{Q}^2 + \overline{U}^2}$ where \overline{Q} and \overline{U} are the average Stokes parameter offsets for the season. Numbers in parentheses denote the corresponding values for the QPC.

^fMeasured channel NET for a typical clear day with K_a -band zenith sky temperature $T_{Atm} \simeq 12$ K. NET measured at Stokes modulation frequency 0.065 Hz.

^gMeasured receiver temperature for each channel.

^g $\simeq 20^\circ$. A comparison of the measured and modelled beams is illustrated in figure 4. The simple Gauss-Laguerre model breaks down at low-power levels, which translates to the far off-axis response of the horn at $\theta \geq 20^\circ$. In the absence of a reliable model for the far off-axis behavior of our feed, we measured the beam response for a variety of frequencies, for both polarizations, as well as the cross-polarization response (see figure 5).

The final component of the feed-horn is the mode converter, which is a separate electroformed element at the throat of the horn. The mode converter combines the TE_{11}° and TM_{11}° circular waveguide modes to create the hybrid HE_{11}° corrugated waveguide mode (Clarricoats & Olver 1984; Zhang et al. 1993). Following the throat in the optical path, there is an electroformed transition from the throat's circular output waveguide to the square-input waveguide of the OMT. This device was designed by matching the cutoff wavelengths of the TE_{10}^\square and the HE_{11}° modes.

3.3. Orthomode Transducer (OMT)

The OMT (variously referred to as a: polarization diplexer, dual-mode transducer, orthomode tee, and orthomode junction) is a waveguide device used to separate the two orthogonal linear polarization states. POLAR's OMT⁸ is a three-port device with a square input port, and two rectangular output ports containing the orthogonal polarization signals.

⁸ Atlantic Microwave: Bolton, MA, Model OM 2800

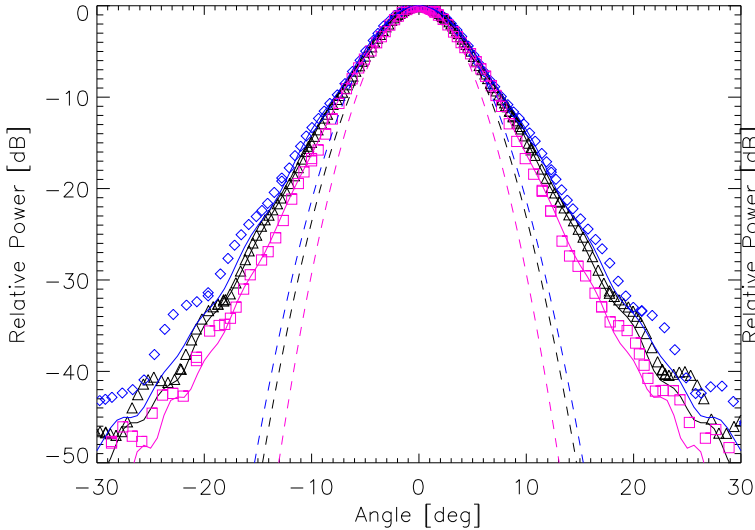


FIG. 4.— Gauss-Laguerre and Gaussian beam models compared to measured beam patterns. The diamonds (26 GHz), triangles (29 GHz), and squares (36 GHz) are the measured beam patterns in the E-plane. The solid lines represent the corresponding Gauss-Laguerre approximations, and the dashed lines are the best-fit Gaussians to the main beam of the measured data.

The OMT's entrance port is K_a -band square guide which simultaneously supports both TE_{01}^{\square} and TE_{10}^{\square} modes. After the modes are separated by the OMT they are further isolated using cryogenic K_a -band isolators⁹. The isolators prevent coupling of the polarization states from reflection by high-VSWR components (such as the HEMT amplifiers). After leaving the OMT the fields in each of the two polarization states are amplified, downconverted, and filtered separately until correlation. POLAR's OMT can be described by a 4×4 scattering matrix, \mathbf{S}_{ij} . Element 1 in the S-matrix refers to the input port with E-plane polarization while 2, 3, 4 refer to input H-plane, output E-plane, and output H-plane respectively. On-diagonal elements of \mathbf{S}_{ij} such as \mathbf{S}_{11} and \mathbf{S}_{22} define the return loss for input E-plane and H-plane polarization states. The terms \mathbf{S}_{13} and \mathbf{S}_{24} determine the co-polar transmission/forward loss, and are not necessarily equal. Differential loss (*e.g.*, $\mathbf{S}_{13} \neq \mathbf{S}_{24}$) will lead to instrumental polarization and/or depolarization. The off-diagonal terms $\mathbf{S}_{34} = \mathbf{S}_{43}$ characterize the output polarization isolation, and the terms \mathbf{S}_{14} and \mathbf{S}_{23} define the OMT's cross-polarization. Plots of the OMT performance are displayed in figure 12. As described in section 5, an offset in the output of the correlation polarimeter can be caused by either non-zero cross polarization or isolation.

3.4. Signal Processing

POLAR's High Electron Mobility Transistor (HEMT) amplifiers (Pospieszalski 1992) provide a gain of ~ 30 dB. POLAR's amplifiers utilize InP based devices for the first stage (which have lower noise-temperatures than GaAs devices) at the expense of slightly increased $1/f$ noise. However, the low-frequency spectral properties of these amplifiers are largely irrelevant for correlation radiometers since

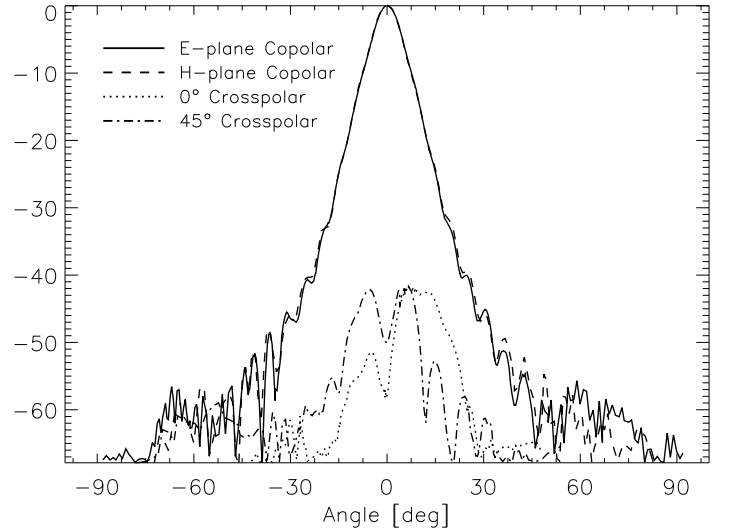


FIG. 5.— Beam maps of the feed-horn measured at 29 GHz are shown. The solid line is the co-polar E-plane power response pattern, the dashed line is the co-polar H-plane pattern, the dotted line is the E-plane cross-polarization response, and the dot-dashed line is the cross-polarization measured at 45° to the E-plane.

the multiplication is performed at several-GHz, *i.e.* well above the few-Hz knee of the HEMTs. POLAR's two amplifiers have noise temperatures of $\simeq 30$ K. Figure 11 shows the low frequency power spectra of the total power radiometer channels (dominated by the HEMTs) compared to the spectra of the correlator channels.

3.4.1. Room Temperature Radiometer Box (RTRB)

After amplification by HEMTs, the RF signals are routed to straight 6 inch long stainless steel waveguides which provide a thermal break from the 20 K HEMTs to the 300 K dewar walls. The stainless guides are bolted to the vacuum-tight WR-28 waveguide feedthroughs. Outside the dewar, straight sections of rhodium plated, brazed-copper waveguides are used to compensate for the path-length differences between the two polarizations incurred by the bends. Finally, the waveguides enter the room temperature radiometer box (RTRB), where the signals are converted from waveguide to coax to match the inputs of the K_a -band warm HEMT amplifiers¹⁰. The noise temperatures of these devices are $T_N \simeq 230$ K.

3.4.2. Superheterodyne Components

Following the second-stage of amplification, the signals are down-converted in frequency from 26-36 GHz to 2-12 GHz by a 38 GHz local oscillator¹¹ (LO) and superheterodyne mixers¹². The IF spectrum is a (scaled) replica of the input RF band, with a nearly identical bandwidth. Two stages of IF (2-12 GHz) amplification are used¹³ to provide the appropriate bias power level into the multipliers. The gain of the IF amplifiers fall steeply above a frequency of

¹⁰ MITEQ: Hauppauge, NY, Model JS426004000-30-8P

¹¹ Millimeter Wave Oscillator Co.: Longmont, CO

¹² MITEQ: Model TB0440LW1

¹³ MITEQ: Model AFS6-00101200-40-10P-6

$f_{3dB} \simeq 12$ GHz. Since each multiplier requires ~ 5 mW of bias power, the IF signal must be amplified by ~ 60 dB. After mixing and IF amplification the signals are divided into two paths. One path, referred to as the ‘total power detector’ channels (TP-E and TP-H) is detected by Schottky diodes¹⁴. ‘E’ and ‘H’ refer to the OMT port in which the respective total power signal originates. The other post-IF gain path is sent into a frequency triplexer¹⁵. The function of the triplexers is three-fold. First they produce three (ideally) independent bands with which are used to investigate the spectral behavior of the data. Secondly, these devices allow us to flatten the gain of the system across the wide RF-bandwidth provided by the HEMTs. Finally, the differential phase between the two arms can be made flatter across the sub-bands than across the full RF band. Prior to correlation the gain and phase of each sub-band are matched with fixed attenuators and phase shifters¹⁶.

3.4.3. Correlators

POLAR’s correlator is a Schottky-diode mixer¹⁷. A mixer-based correlator is composed of a double balanced mixer, a phase modulating element, and lock-in detection. The primary difference between a multiplier and a conventional mixer is that the IF bandwidth of the multiplier is made intentionally narrow to suppress frequency components greater than ~ 100 MHz, and the output of the multiplier can support DC.

The RF band passes of the multipliers are from 1-12 GHz and the IF bandpasses are from 0-100 MHz. The IF output port is not transformer-coupled, and propagates the DC signal proportional to the correlation between signals in the x and y polarization states. Phase modulation and phase-sensitive detection (PSD) is accomplished by an electronic $0^\circ - 180^\circ$ phase shifter¹⁸, and a synchronous demodulator¹⁹ and integrator. The phase of the LO is switched between 0° and 180° at 1 kHz prior to mixing the E_y^{RF} waveform. The voltage produced by the correlators at this stage switches between $\kappa E_x^{RF} E_y^{RF}$ and $-\kappa E_x^{RF} E_y^{RF}$ at 1 kHz, where κ is the intensity-to-voltage conversion factor determined during calibration (section 4). The output of the lock-in detectors is proportional to the correlated component in each arm of the polarimeter.

Two lock-in detectors per correlator are used: one in-phase with the phase shifter modulation, and the other for the component 90° out of phase. The latter are referred to as quadrature phase channels (QPC), and are used as noise monitors as discussed below. Signals leave the pre-amp card and enter a separate RF-tight box containing six separate lock-in circuits, corresponding to phase sensitive detection of three correlators, each with two reference phases, “in-phase” and “quadrature-phase”. The demodulated signal is low-pass filtered at 5 Hz.

3.4.4. Post-Detection Electronics

¹⁴ Hewlett Packard: Model HP 8474C

¹⁵ Reactel Corp.: Gaithersburg, MD

¹⁶ Weinschel Corp.: Model 917-22

¹⁷ MITEQ: Model DBP112HA

¹⁸ Pacific Millimeter Products: Golden, CO

¹⁹ Analog Devices: Model AD 630

The pre-amplifier is the final component of the signal chain for the total power detectors, and the penultimate component for the correlators (as these are post-detected via the lock-in circuits described above). To minimize the susceptibility to electromagnetic interference (EMI), the signals are amplified and filtered before leaving the radiometer box. A single circuit board contains five (two total power channels, three correlator channels) circuits. The card is mounted $\simeq 3$ inches from the correlators and shares the same thermally regulated environment. The first stage of the post-detection electronics is a low noise pre-amplifier. Following the gain stage is a 4-pole, 5 Hz anti-aliasing filter²⁰. The bandpass of the anti-aliasing filter also sets the fundamental integration time, τ .

3.4.5. Electronics Box and Housekeeping

Thermal regulation of the RTRB is essential to the stability of the instrument over long periods of time. The most temperature sensitive components are the non-linear devices such as the mixers, multipliers, and especially the Gunn oscillator. The temperature coefficient of the oscillator output was $\sim 1 \text{ mW K}^{-1}$ and the gain following the oscillator was ~ 20 dB. The correlators required 5 mW of bias power so the oscillator’s temperature was kept stable to $\sim 10 \text{ mK hour}^{-1}$ resulting in a maximum bias power change of $\sim 0.3\%$ per rotation of the polarimeter. To regulate the temperature, a closed-loop thermal control circuit using feedback from a sensor inside the RTRB was constructed. This circuit used a commercial microprocessor-based PID controller²¹, and was capable of regulating up to 300 W of power applied directly to six 25 W heater pads²². Several other housekeeping signals, including temperature sensor diodes inside the cryostat (on the HEMTs, 20 K cold plate, and feed horn) and the dewar pressure are monitored. A multi-stage power regulation approach is implemented. This system employs precision voltage regulators and references throughout the RTRB; all signal circuitry (HEMT bias cards, post-detection electronics, etc.) are voltage regulated and EMI shielded.

3.4.6. Data Acquisition

The data acquisition system is composed of an analog-to-digital converter²³, and a notebook computer running National Instruments Labview software. The 16 bit analog-to-digital converter (ADC) samples all 8 data channels as well as 8 housekeeping channels at 20 Hz. By digitizing all of the data in close physical proximity ($\simeq 10$ in) to the detectors, potential EMI contamination is reduced. The rotation angle is indexed by a 12 bit relative angular encoder and a one-bit absolute angular encoder (once per 360° rotation). The data files are indexed by calendar time and date, with several hundred files stored per day. After 7.5 minutes of acquisition, the files are transferred from the notebook computer (located on the rotation platform) to a desktop computer via a local area network Ethernet connection. The coax Ethernet connection leaves the rotating electronics box through 2 channels of a 10 channel shielded slip-ring.

²⁰ Frequency Devices: Haverhill, MA

²¹ Omega Inc.: Stamford, CT

²² MINCO: Minneapolis, MN

²³ National Instruments DIO-MIO-16 Daqpad

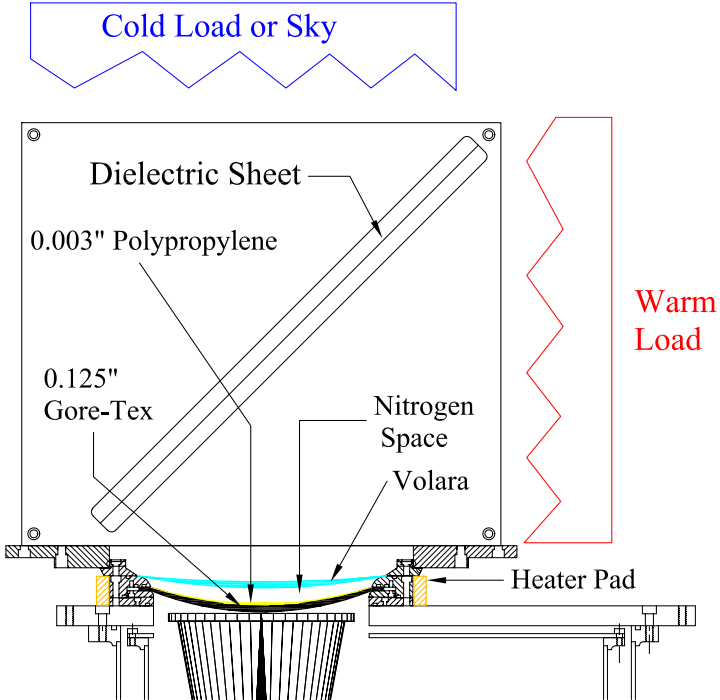


FIG. 6.— Side view of window and calibrator configuration. The calibrator grids (either the wire grid or the dielectric sheet - Section 4) mount on a rotation bearing attached to the window flange. The calibrators fill the beam and rotate around the horn axis. For both the dielectric sheet and the wire grid calibrators, hot and cold loads are used to generate $\sim 100\%$ polarized sources, ranging from 20 mK (dielectric sheet) to 200 K (wire grid).

3.5. Vacuum Window

A multi-element vacuum window (figure 6) is composed of a 0.003 inch vacuum-tight polypropylene vacuum barrier and a 0.125 inch (permeable) Gore-Tex²⁴ layer which supports the atmospheric load on the window. A layer of Volara²⁵ (expanded polyethylene) seals in a dry-nitrogen gas layer between the polypropylene and prevents condensation and ice on the vacuum window. A resistive heater element wrapped around the vacuum window flange warms the window to ~ 27 C to reduce the formation of dew. With this window the dewar pressure remains below 10^{-6} Torr for months at a time. The emission from the window is estimated to be $\lesssim 20$ mK, and the reflected power coefficient is $\lesssim 1\%$.

3.6. Ground Screens

POLAR uses two concentric ground screens; one co-rotating with the receiver, the other fixed to the observatory structure (see figure 7). The use of two ground screens is not unusual in the field, although POLAR's screens are designed to reject polarized beam spillover, rather than unpolarized, total-power spillover. The inner ground screens are designed to terminate the side-lobe power in a known temperature source and absorb, rather than reflect, solar and lunar light. The inner conical ground screen is covered with 0.5 inch Eccoisorb foam designed to suppress specular reflection²⁶. This absorptive approach is uncommon

in CMB anisotropy experiments as it increases the total power loading on the detectors. However, the increase in system temperature due to the inner shield is estimated to be $\lesssim 1$ K. The absorption of the foam is greater than 30 dB, and the estimated induced polarization is estimated to be $< 0.5\%$ leading to a maximum polarization produced by the foam of < 1 mK. The analogous figure for a metallic screen would be ten to one hundred times larger. Since the inner ground screen co-rotates with the receiver, it will only produce a constant offset to which the instrument is insensitive.

The second level of shielding is of the more conventional reflective-scoop design, *e.g.* Wollack et al. (1997), and is designed as a sun-shade for the inner shield. The scoop is mounted to the side of the POLAR observatory, and is made of four aluminum panels, 8' wide and 4.8' high. The level of sidelobe suppression is estimated using Sommerfeld's scalar diffraction theory for points deep in the shadow region of a knife-edge scatterer (Jackson 1975). The estimated suppression is $\simeq -40$ dB, which in combination with a similar (measured) figure from the inner ground screen, and the sidelobe response of our feed horn, gives a total estimated sidelobe suppression better than -100 dB. The response at 90° off-axis relative to the peak forward gain was measured to be < -50 dB using a polarized source transmitting in the K_a -band from various locations around the instrument enclosure. As discussed in section 5.4, the square shape of the scoop is thought to have produced a $\sim 100 \mu\text{K}$ offset in the Stokes parameters.

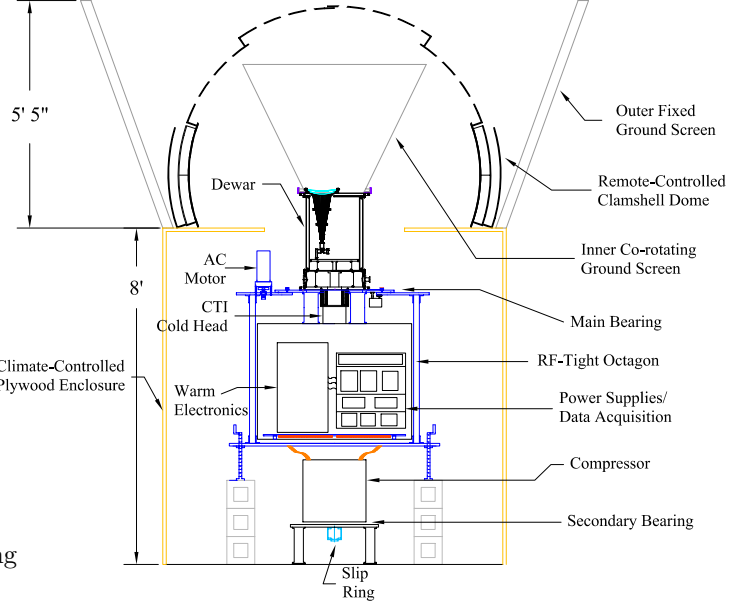


FIG. 7.— POLAR observatory and ground screens. Two sets of ground screens are used to reduce the polarized spillover from the earth, as well as polarized emission from the shields themselves. The outer shield is fixed to the structure in which POLAR resides, and is composed of a lightweight steel skeleton covered by 0.05" aluminum sheets. The inner ground screen is covered with flat Eccoisorb panels, and co-rotates with the radiometer. Also shown is the motor-driven, fiberglass clamshell-dome which is remotely operated via the World Wide Web in the event of inclement weather. The rotation mount, drive motor, bearing, and angular encoder are also shown.

²⁴ W.L. Gore & Associates: Newark, DE

²⁵ Voltek Corp.: Lawrence, MA

²⁶ Emerson & Cuming: Randolph, MA, Product LS-26

3.7. Rotation Mount and Drive System

Measurement of the Stokes parameters is dependent on signal modulation under rotation. POLAR employs a 30 inch diameter bearing and AC motor system to rotate the cryostat at 2 RPM (~ 33 mHz). An AC motor produced smoother motion than several stepper motors tried initially, and was chosen for continuous rotation. The dewar rides on a bearing composed of two plates each with a 0.100 inch wide channel filled with ~ 400 stainless-steel ball-bearings. The motor pulley has a 12 bit relative angle encoder which reads out the rotation angle. In addition, a one-bit absolute encoder is triggered once per revolution and this defines the zero angle of the instrument frame. In order to decouple the vibrations produced by the cryocooler compressor from the receiver, a separate, vibration isolated rotation mount is used to support the compressor. The second bearing is loosely coupled to the main rotation bearing/AC motor drive using braided copper straps. Power and ethernet connections interface with the rotating system via the 10 channel slip ring. The mount is not steerable, so POLAR is restricted to zenith scans.

3.8. Instrument Bandpasses

Laboratory measurement of the room temperature radiometer box bandpasses used an HP 83751A Synthesized Sweeper and an active frequency doubler to produce a swept signal from 26 - 36 GHz and fed into a power splitter. The outputs from the power splitter were 100% correlated, and these signals were fed into the waveguide input ports of the RTRB. The bandpasses of the three correlator channels are shown in figure 8 and the bands for all channels, including the total power channels, are listed in table 1. For the correlator channels these bands include the effects of phase decoherence.

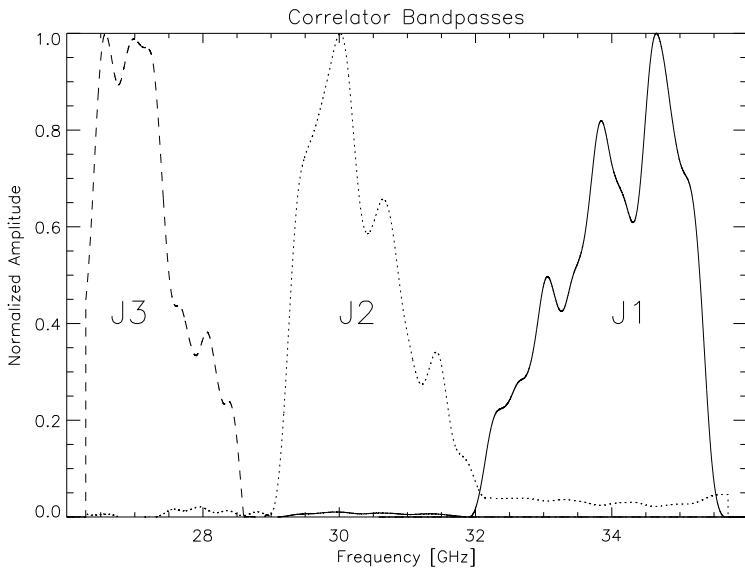


FIG. 8.— Bandpasses of all three correlator channels are shown, not including the HEMT amplifier response. A K_a -band correlated signal is injected into each arm of the warm electronics, and the signal frequency is swept from 26 to 36 GHz to measure the bandpasses.

3.9. Receiver Noise and Sensitivity

Three methods were used to measure POLAR's noise temperature. Y-factor measurements (Pozar 1990) of the total power channels were performed with both a cooled internal calibrator (which is accurate, but does not include the effects of the feed-horn) and an ambient temperature external load (which is faster, but requires a larger dynamic range) to ensure consistency. The ambient temperature loads used were 300 K, 77 K, and the sky ($\simeq 12$ K, zenith).

In addition to the two y-factor methods T_{rec} was inferred from noise measurements. Given the instrument bandwidth $\Delta\nu$, the voltage fluctuations ΔV_{rms} in an integration time τ , and the calibration coefficient, g in [V/K], the noise temperature of the receiver can be estimated using the radiometer equation:

$$T_{rec} = \frac{g^{-1}}{\kappa} \Delta V_{RMS} \sqrt{\Delta\nu\tau} - T_{load}, \quad (11)$$

where $\kappa = 1$ for the total power channels, and $\kappa = \sqrt{2}$ for the correlator channels. The noise equivalent temperature (NET) of the radiometer is related to the RMS temperature fluctuations via $\Delta T_{rms} = NET/\sqrt{\tau}$. For both the total power channels and the correlators ΔT_{rms} is a linear function of the load temperature. The x-intercept of these lines is equal to the negative of the system noise temperature.

The system noise temperature is dominated by the noise temperature of the HEMT amplifiers which are $\simeq 30$ K for both amplifiers. However, the contribution of the room-temperature amplifiers, as well as loss in components preceding the HEMTs, cannot be neglected. The dominant lossy elements preceding the HEMTs are the cryogenic isolators and the dewar's vacuum window. The isolators' exact physical temperature is unknown, but estimated to be $\lesssim 40$ K, which is the physical temperature of the horn, so this is a worst-case estimate. Their insertion loss is 0.1 dB. The loss of the vacuum window is conservatively estimated at 1%. The room temperature RF amplifiers have noise temperatures of 232 K. The total estimated system noise temperature including all factors is $T_{sys} = 46$ K. Table 1 displays the noise temperatures of all channels using the linear intercept (noise) method outlined above. Some compression was discerned for the highest ambient temperature load used (300 K). Correlator J3 exhibits the highest level of compression, has the largest OMT insertion loss, has the smallest bandwidth and obtains the highest NET.

The three methods used to estimate the receiver noise temperature of the total power channels (internal load, external load and noise fluctuation method) agree to within ~ 5 K. In the field, the external load method was used to track the noise temperatures on a daily basis. Using liquid nitrogen and the sky for the loads, no compression was observed in any channel. For the correlator channels, only the noise temperatures estimated from the noise method were used. Noise temperatures for all channels are displayed in table 1.

4. CALIBRATION

A calibration accurate to $\simeq 10\%$ was deemed necessary for POLAR given the expected signal levels at large angular scales. This goal was achieved for all correlator chan-

nels with an absolute calibration method. An ideal calibration source would be a polarized astrophysical point source with enough power to be seen in “real-time”. For illustration, we compute the power needed to produce a 5σ detection in a 1 second integration – bright enough to detect in real-time. The antenna temperature seen by POLAR’S total power detectors when viewing a source of flux density S_ν is $T_{ant} = 2.8 S_\nu \frac{\mu\text{K}}{\text{Jy}}$. POLAR’S NET $\simeq 1 \text{ mK s}^{1/2}$, so a source of antenna temperature $T_{ant} \simeq 5 \text{ mK}$ is required for a 5σ detection in one second. This is equivalent to a $\sim 1700 \text{ Jy}$ source. For comparison, Cas-A, the brightest known radio source, has a flux density of only $194 \pm 5 \text{ Jy}$ at 32 GHz (Mason et al. 1999). Since Cas-A is less than 10% polarized at 32 GHz, the polarized signal is smaller still. Clearly, no astrophysical sources were suitable for POLAR’s calibration. In addition, the rotation mount is not pointable, so POLAR can only observe sources at zenith transit. Instead, polarized signals were created by reflection of black-body emission from wire grids (in-laboratory calibration) and dielectric sheets (during the observing campaign).

4.1. Wire Grid Calibrator

Two methods of calibration were used, depending on the dynamic range required for the measurement. Initially, a wire grid was used to test the receiver in the lab and to probe instrumental polarization and cross-polarization behavior. The grid produces a highly polarized ($> 99\%$), bright ($T_{ant} = 200 \text{ K}$) signal. The limited dynamic range of the receiver does not allow the wire grid to be used as a calibrator when the instrument is in its observing (highest gain) configuration. However, the grid was extremely useful for characterizing the polarimetric fidelity of the receiver.

Wire grid calibrators (WGC) are useful for near field polarization calibration (Chu 1975; Lubin & Smoot 1981; Gasiewski & Kunkee 1993). The WGC produces correlated electromagnetic fields in each arm of the receiver, and is placed outside the cryostat for rapid implementation. The grid (figure 6) transmits thermal radiation from a black-body source in one polarization, and reflects thermal radiation from a second black-body source (at a different temperature) into the orthogonal polarization. For the POLAR calibrator, the cold load is located above the grid and produces electric fields E_1 and H_1 , and the warm load produces fields E_2 and H_2 . E and H refer to the orthogonal electric field components produced by the two loads. Ideally, H_1 is transmitted and E_2 is reflected into the feed-horn producing a $\simeq 100\%$ polarized diffuse source with an antenna temperature approximately equal to the thermodynamic temperature difference between the two loads.

The wire-grid calibrator was fabricated by deposition of copper onto a 24 inch \times 24 inch *times* 0.002 inch mylar substrate. The wires are 0.008 inch wide with 0.008 inch pitch. For support the grid is sandwiched between Dow Corning “pink” Styrofoam sheets (emissivity $\leq 1\%$), and the sandwich is mounted at 45° to the aperture plane (figure 6). The grid has an integrated bearing system which allows it to rotate directly over the vacuum window and feedhorn.

The correlator output voltage depends on the coherence

of the electric fields produced by the thermal radiators. However, only the antenna temperatures of the hot and cold loads are known, not the electric fields produced in the x and y directions. Fortunately, as shown below, only the antenna temperatures are needed. The field input to the feed-horn is $\vec{H}_1 + \vec{E}_2$. In terms of the (x', y') basis of the feed-horn and OMT and the (x, y) basis of the rest frame of the WGC, the magnitude of the electric fields E and H produced by the WGC as the grid is rotated (about the vertical) with respect to the polarimeter by an angle α is:

$$E_{x'} = E_x \cos \alpha + E_y \sin \alpha$$

$$E_{y'} = -E_x \sin \alpha + E_y \cos \alpha.$$

Since the load fills the antenna far-field beam (edge taper $> 20 \text{ dB}$), the output of the correlator from the coherence function given by equation 9 is:

$$V_{out} \propto \langle \hat{E}_{x'}(\nu) \hat{E}_{y'}^*(\nu) \rangle$$

$$= \langle (E_x \cos \alpha + E_y \sin \alpha)(-E_x^* \sin \alpha + E_y^* \cos \alpha) \rangle.$$

Performing the multiplication, we obtain:

$$V_{out} \propto \langle -E_x \cos \alpha E_x^* \sin \alpha + E_y \sin \alpha E_y^* \cos \alpha \rangle$$

$$= \langle E_y E_y^* - E_x E_x^* \rangle \sin \alpha \cos \alpha$$

$$= Q \sin 2\alpha = \gamma(T_y - T_x) \sin 2\alpha$$

where γ converts antenna temperature (measured by the radiometer) to intensity (the units of the Stokes parameter).

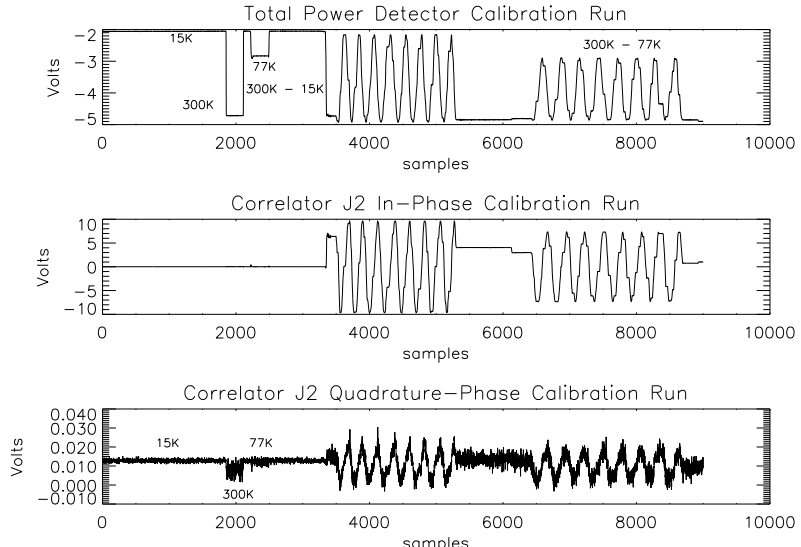


FIG. 9.— Calibration Run for Correlator Channel J2 and TP-E. Voltages out of correlator J2 and total power detector TP-E (top figure) during calibration with the wire grid calibrator are displayed. Output from TP-E is 90° out of phase with respect to the correlator channels. TP-E uses a negative polarity total power detector. The middle figure shows the voltage out of J2’s in-phase lock-in detector, the bottom figure shows the corresponding voltage out of J2’s quadrature phase lock-in detector. The various temperature loads are indicated at the time they are applied. The first set of oscillations corresponds to a polarized signal obtained using a 300 K load (reflected) and the sky (transmitted), which produces a $\sim 260 \text{ K}$ signal. The second set of oscillations corresponds to a polarized temperature obtained by using a 300 K load and a liquid nitrogen load producing a $\sim 190 \text{ K}$ signal. The output of the quadrature phase detector is suppressed by $\sim 30 \text{ dB}$ relative to the in-phase channel. The noise envelope of the J2 QPC detector is a function of the load temperature since the correlator acts like a negative polarity power detector and is thus useful as a noise monitor.

ter, Q). Note that at $\alpha = 0^\circ, 90^\circ, 180^\circ, 270^\circ$ the correlators have zero output as the fields are completely aligned along one axis of the OMT. Ideally, the grid would reflect T_{hot} from the side in 100% horizontal polarization and transmit T_{cold} from the top in 100% vertical polarization, resulting in

$$V_{out} \propto \gamma(T_{cold} - T_{hot}) \sin 2\alpha. \quad (12)$$

In practice, due to loss and reflection, the following antenna temperatures are observed at the feed-horn in the two orthogonal polarizations (Gasiewski & Kunkee 1993):

$$\begin{aligned} T_{hot'} &= r_{||}[(1 - r_l)T_{hot} + r_lT_{bg}] + \\ &\quad (1 - r_{||})[(1 - r_l)T_{cold} + r_lT_{bg}] \quad (13) \\ T_{cold'} &= t_{\perp}[(1 - r_l)T_{cold} + r_lT_{bg}] + \\ &\quad (1 - t_{\perp})[(1 - r_l)T_{hot} + r_lT_{bg}], \end{aligned}$$

where $r_{||}$ is the grid reflection coefficient for radiation polarized parallel to the wires, t_{\perp} is the grid's transmission for radiation polarized perpendicular to the wires, r_l is the reflection coefficient of the load, and $T_{bg} = T_{hot}$ is the effective background temperature surrounding the calibrator. In the above equations, the effects of the emissivities and dielectric constants of the mylar and Styrofoam have been neglected.

Two pairs of temperature differences were used to characterize POLAR. Using a 300 K load (in reflection) and the sky (in transmission) a polarized antenna temperature of 256 K is obtained. Using a 300 K load (in reflection) and a 77 K Liquid Nitrogen load (in transmission) an antenna temperature of 196 K is obtained. The following properties of the grid were calculated using Fresnel's equations and measured indices of refraction (Goldsmith (1998) and references therein): parallel polarization reflectivity $r_{||} = 0.995$, perpendicular polarization transmissivity $t_{\perp} = 0.95$, load reflectivity $r_l = 0.02$. A plot of a calibration run is shown in figure 9.

4.1.1. Gain Matrices

Following Gasiewski & Kunkee (1993) the output of the polarimeter versus rotation angle is modelled as a linear combination of the Stokes parameters at the feed horn. The three output voltages from the two total power detectors and a correlator are modelled as a vector:

$$\mathbf{v} = \hat{\mathbf{g}}\mathbf{T}_F + \mathbf{o} + \mathbf{n} \quad (14)$$

where $\hat{\mathbf{g}}$ denotes the 3×3 gain matrix, $\mathbf{T}_F = (\mathbf{T}_c, \mathbf{T}_h, \mathbf{T}_c - \mathbf{T}_h)$ is the vector of input antenna temperatures produced by the grid, and \mathbf{o} and \mathbf{n} represent offset and noise contributions to \mathbf{v} respectively. The coordinate basis of \mathbf{v} is defined by the OMT. For simplicity we only consider the coupling of one correlator to the total power channels, so the dimension of the system is 3 rather than 5 for POLAR. Ideally, $\hat{\mathbf{g}}$ would have only on-diagonal elements, however the off-diagonal elements of $\hat{\mathbf{g}}$ correspond to various non-idealities of the instrument which will result in offsets in our measurements.

As the grid rotates, the resulting vector of voltages is recorded and a least-squares fit is made to the data using the radiometer model of equation 14. The gain matrix parameters, including the off-diagonal cross-talk elements, and the offsets are recovered for each calibration run. With the antenna temperatures of the loads given by equation

13, the voltages out of the two total-power channels and the correlator channel are:

$$\mathbf{v} = \begin{pmatrix} g_{yy}T_c + g_{yx}T_s + g_{yQ}(T_{hot'} - T_{cold'}) \sin 2\alpha + o_y \\ g_{xy}T_c + g_{xx}T_s + g_{xQ}(T_{hot'} - T_{cold'}) \sin 2\alpha + o_x \\ g_{yQ}T_c + g_{xQ}T_s + g_{QQ}(T_{hot'} - T_{cold'}) \sin 2\alpha + o_Q \end{pmatrix} + \mathbf{n} \quad (15)$$

where

$$T_c = T_{hot'} \cos^2 \alpha + T_{cold'} \sin^2 \alpha$$

and

$$T_s = T_{hot'} \sin^2 \alpha + T_{cold'} \cos^2 \alpha.$$

To recover $\hat{\mathbf{g}}$, we first integrate long enough that the noise term, \mathbf{n} , is negligible, and then average the offsets, \mathbf{o} , as a function α and subtract them. Then equation 15 is inverted to obtain $\hat{\mathbf{g}}$. The on-diagonal elements (g_{xx}, g_{yy}, g_{QQ}) of $\hat{\mathbf{g}}$, dominate the matrix; they are the terms which measure the system calibration in [V/K]. Typical values are $\sim (100 \text{ K/V})^{-1}$. The off-diagonal elements encode the system's gain imbalance, cross-talk, and imperfect isolation between polarization states. The g_{xy} terms are approximately 1% of the g_{xx}, g_{yy} terms, and the g_{xQ}, g_{yQ} terms are $\leq 1\%$ of the g_{QQ} terms for all three correlators.

There are two classes of systematic effects which lead to the off-diagonal elements $g_{xy} = g_{yx}$ and $g_{xQ} = g_{yQ}$. To analyze the effects of $g_{xy} \neq 0$, we set $g_{yQ} = n_y = o_y = 0$, and identify the first non-ideality, g_{xy} (which is equal to g_{yx}). This implies that at $\alpha = 0$, when only $T_{hot'}$ should be observed, $v_y = g_{yy}T_{hot'} + g_{yx}T_{cold'}$ is observed. Thus, g_{xy} terms represent cross-polarization. The main contribution to the correlator offset is from cross-polarization of the OMT and/or imperfect isolation of the OMT. The off-diagonal elements, *e.g.*, g_{xQ} , are attributed to gain differences in the feed horn's E and H plane power response, and can be equalized in hardware or software.

Since two pairs of temperature differences (300 K load vs. 77 K load and 300 K load vs. the sky) were used, the calibration constants as a function of the temperature difference were measured and checked for linearity. The two pairs of loads produced effective polarized antenna temperatures of 256 K and 196 K, and it was verified that the calibration constants were equal to better than 10% over this range for J1 and J2.

4.2. Dielectric Sheet Calibrator

As mentioned above, calibrations performed during the observing campaign did not use the wire grid calibrator. The primary reason for this was the limited dynamic range of the polarimeter; both the last stage of IF amplifiers and the correlators themselves began compressing when the antenna temperature was ~ 100 K in the observing (high gain) configuration. When the sky was the cold load, a full rotation of the wire grid produces a modulated signal with amplitude $100 \text{ K} < T_{ant} < 250 \text{ K}$. The variation in bias power to the correlators produced by the WGC as it was rotated was significant. The largest imbalance loaded the correlators with 40 K on one port and up to 290 K on the other port. This imbalance is undesirable and was the initial reason the Dielectric Sheet Calibrator (DSC) was used (O'Dell et al. 2002a). During observations, the calibrator should produce a total power load similar to the sky loading, which is only slightly polarized.

During the observing campaign, the wire grid calibrator was replaced by a thin (0.003 inch) polypropylene film. This produces a signal that is only partially polarized. The polarized signal produced by the (DSC) is

$$Q = [(T_{hot} - T_{cold})(R_{TE} - R_{TM}) + (T_S - T_{cold})(\epsilon_{TE} - \epsilon_{TM})] \cdot \sin 2\alpha \quad (16)$$

where T_S is the physical temperature of the dielectric sheet. ϵ_{TE} is the emissivity of the dielectric in the TE polarization state (perpendicular to the plane of incidence), and ϵ_{TM} is the emissivity in the TM polarization state (parallel to the plane of incidence). Note that this expression reduces to equation 12 in the wire grid case, where $R_{TE} - R_{TM} = 1$, and $\epsilon_{TE} = \epsilon_{TM} = 0$.

The reflection coefficients of the DSC is determined by the dielectric constant and the geometry:

$$R = \frac{[\cos^2 \theta - \gamma_i^2]^2 \sin^2 \delta}{4\gamma_i^2 \cos^2 \theta \cos^2 \delta + [\cos^2 \theta + \gamma_i^2]^2 \sin^2 \delta} \quad (17)$$

where $i \in \{TE, TM\}$, and

$$\gamma_{TE} \equiv \sqrt{n^2 - \sin^2 \theta} \quad (18)$$

$$\gamma_{TM} \equiv \frac{1}{n^2} \sqrt{n^2 - \sin^2 \theta} \quad (19)$$

$$\delta = 2\pi\nu t \sqrt{n^2 - \sin^2 \theta}, \quad (20)$$

where n is the refractive index of the sheet, ν is the frequency, t is the sheet thickness, and θ is the angle of incidence of the incoming radiation. For our geometry, $\theta = 45^\circ$.

For 0.003 inch polypropylene at 30 GHz, $R_{TE} - R_{TM} \approx 0.2\%$. The emission from the sheet is ~ 4 mK per 0.001 inch of thickness, and is negligible compared to the reflection-induced signal. When the sky is used as the cold load and a 300 K hot load is used, $T_{hot} - T_{cold} \approx 260$ K, and produces a rotation modulated polarized calibration signal of ~ 500 mK, and an unpolarized background power of ~ 10 K (the sky temperature).

Equation 17 was verified in laboratory tests; the results for 0.003 inch polypropylene are given in Figure 10. The primary sources of error in our final calibration were uncertainties in the indices of refraction and the slight thickness variations in the sheet; these 5% variations lead to final calibration error of 8.5% for J1 and J2, and 11% for J3.

5. SYSTEMATIC EFFECTS AND RADIOMETRIC OFFSETS

5.1. System Sensitivity Degradation

Once the conversion between voltage and temperature is known, by measuring the voltage RMS the temperature RMS can be obtained. The noise in an arbitrary integration time, τ , is $\Delta T_{RMS} = NET/\sqrt{\tau}$. The most naive technique to obtain the NETs is simply to calculate the RMS of the time stream in a one-second segment and convert from voltage to temperature. This approach, however, over-estimates the NET, and only applies when the noise is white (no $1/f$ noise). A general expression for the post-detection spectral density of correlation and total power radiometers which includes the effects of gain fluctuations, $\Delta G(f)$, a system offset, T_{offset} , and offset fluctuations, $\Delta T_{offset}(f)$, is given by (Wollack 1995; Carretti et al. 2001):

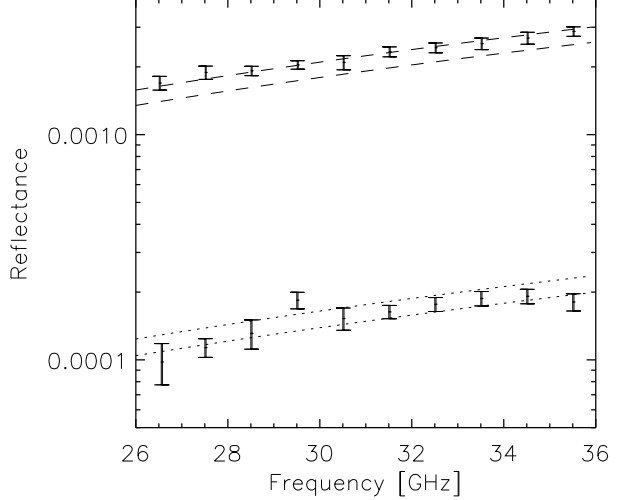


FIG. 10.— Comparison between laboratory reflectivity measurements and theory on 0.003 inch polypropylene situated at $\theta = 45^\circ$. Errors in the data are mostly systematic, arising from standing waves in the system. The uncertainty in the model is due to both thickness variations and uncertainties in the index of refraction of the dielectric sheet. R_{TE} corresponds to the upper set of curves (dashed), and R_{TM} to the lower set of curves (dotted).

$$P^{\text{corr}}(f) = 2 \frac{\kappa^2 T_{sys}^2}{\Delta\nu} + T_{offset}^2 \Delta G^2(f) + \Delta T_{offset}^2(f), \quad (21)$$

$$P^{\text{TP}}(f) = 2 \frac{T_{sys}^2}{\Delta\nu} + T_{sys}^2 \Delta G^2(f) + \Delta T_{sys}^2(f). \quad (22)$$

Note that the second and third terms of equations 21 and 22 do not depend on the RF bandwidth, $\Delta\nu$ and do not, in general, integrate down with time. The audio frequency, f , dependence of the gain fluctuations for the HEMT amplifiers is $\Delta G(f) \propto f^{-1}$ (Wollack 1995). These equations, along with Figure 11 (which shows the power spectra of all three in-phase correlator channels and both total power detectors during an observation run) illustrate the relative performance tradeoffs of the total power polarimeter versus the correlation polarimeter. POLAR uses both types of radiometer; however, the total power polarimeter channel is used only as an atmospheric monitor. The instantaneous difference between the two total power channels (TP-E and TP-H) is proportional to the Stokes Q parameter in the OMT frame, and after 45° rotation would provide the U parameter. However, for a total power receiver the HEMT gain fluctuation noise $\Delta G(f)$ in equation 22 multiplies the *system* temperature ($T_{sys} = T_{rec} + T_{ant}$) rather than the *offset* temperature as in equation 21. This produces the dramatic $1/f$ rise in the total power detectors' PSD, which is greatly diminished for the correlator channels. This allows us to slowly modulate the signal by rotation of the radiometer at 33 mHz, rather than at several Hz as would be required for the total power channels. It is clear from the spectra that the correlators are far more sensitive and stable than the total power detectors.

The correlation radiometer offset is produced by signal power which is correlated between the two polarization states. This effect is primarily the result of non-zero cross

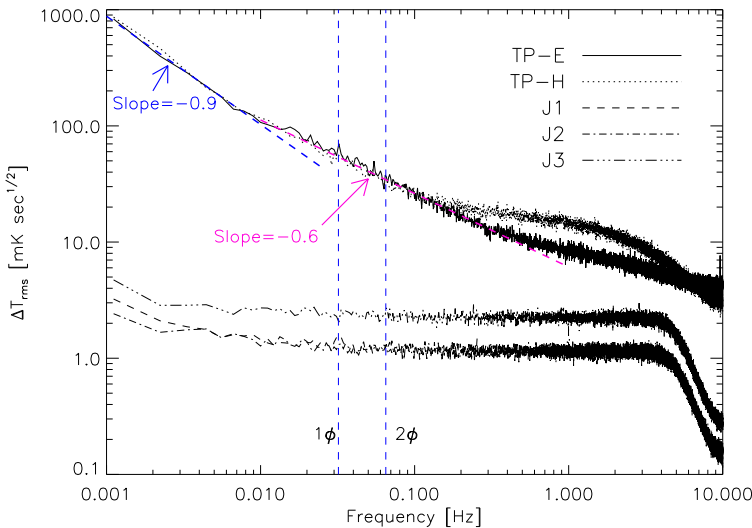


FIG. 11.— Square-root power spectra of all five POLAR signal channels. The $1/f$ behavior of the total power detectors, and the low-pass anti-aliasing filters are evident. The CTI coldhead expansion/compression cycle is at 1.2 Hz, and no contamination is observed in the signal channels. Vertical lines indicate the rotation frequency (1ϕ) and the Stokes parameter modulation frequency (2ϕ). The low frequency rise in the total power detector spectra is due to both HEMT gain fluctuations (for $f > 0.01$ Hz) and atmospheric fluctuations (for $f < 0.01$ Hz). A “ $1/f$ ” fluctuation spectrum has a slope of -0.5 on this plot and a Kolmogorov atmospheric fluctuation spectrum has a power law slope of $\simeq -1.3$. The low frequency rise in the correlator spectra at $f < 0.01$ Hz has a power-law slope of ~ -1 which indicates that it arises from atmospheric fluctuations. Correlator J3 has a smaller bandwidth and higher isolator loss than J1 or J2 leading to a higher white noise level. The anti-aliasing filter on TP-H had a low-pass cutoff at 5 Hz (identical to the correlators), while TP-E’s low-pass cutoff was at 50 Hz leading to different spectral shapes.

polarization and polarization isolation of the OMT. The total spurious polarization generated by the OMT is due to both cross polarization and imperfect isolation. In Figure 12 the isolation, cross polarization, insertion loss, and return loss are shown.

Since the correlation polarimeter offset is produced mainly by spurious polarization of the OMT, the dominant source of offset fluctuations will be from fluctuations in the antenna temperature of observed sources, primarily (unpolarized) atmospheric emission: $T_{offset}(f) = SP_{omt}T_{atm}(f)$, where SP_{omt} is the OMT’s spurious polarization (sum of the isolation and cross-polarization). The OMT’s cross-polarization dominates the spurious polarization, since the total isolation between the polarization states is the sum of the isolation of the OMT and cryogenic isolators on the output ports of the OMT. The total isolation is < 50 dB. In addition, path length differences in the two arms leads to phase decoherence for signals reflecting off the HEMT amplifiers and propagating in the reverse direction. This reduces the effects of non-zero isolation to negligible levels. The atmospheric component of antenna temperature fluctuations at 30 GHz follows a Kolmogorov spectrum which falls as $T_{atm}(f) \propto f^{-8/3}$ (Carretti et al. 2001). If the experiment is not modulated at a frequency much higher than the knee frequency of the fluctuation spectrum, these terms will dominate the system NET. To perform this modulation POLAR was rotated at 0.033 Hz. Figure 11

shows the power spectra produced by all radiometer channels, including the effects of atmospheric fluctuations.

The stability of the offsets over a single rotation of the instrument is crucial to the recovery of the Stokes parameters. Note that the behavior of the noise should be independent of the phase of the reference waveform supplied to the phase-modulation lock-in detectors. The QPC are insensitive to correlated signals, including uncorrelated atmospheric emission which is spuriously correlated by the OMT. The QPC therefore show almost no $1/f$ noise; residual $1/f$ noise at the $\simeq -25$ dB level is due to cross-talk in the low frequency electronics and the inability to perfectly match the phase in each arm. The QPC proved to be powerful monitors of the intrinsic noise of the radiometer. Over the course of the 2000 observing campaign, we found periods of high offset and large offset fluctuations to be correlated with environmental effects, especially the occasional formation of dew and ice on the vacuum window.

5.2. Optical Cross Polarization

The corrugated scalar feed horn demonstrates low cross-polarization(Clarricoats & Olver 1984). However, even for an ideal and completely symmetric feed there is always non-zero cross-polarization. For an ideal horn, the cross-polarization induced by scattering in a plane containing the polarization axis is identically zero since there has been no polarization conversion. This is also manifestly true for scattering in a plane perpendicular to the polarization axis. However, using a simple geometric optics approximation it can be demonstrated (Clarricoats & Olver 1984) that there is polarization conversion (cross-polarization) which varies as $\sin^2 \phi$, and will be peaked at $\phi = 45^\circ, 135^\circ, 225^\circ, 315^\circ$ where ϕ is the azimuthal angle in the aperture plane. The maximum cross-polarization

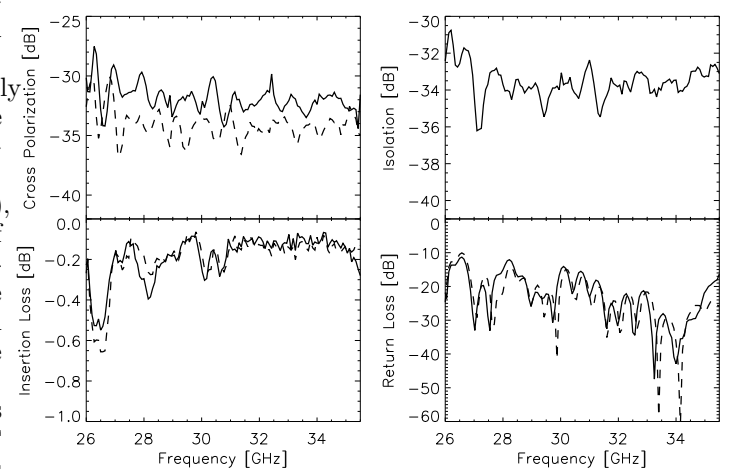


FIG. 12.— Properties of POLAR’s OMT. Isolation, cross-polarization, return loss, and insertion loss are shown across the K_a band. For the insertion and return loss plots, the solid line is for the E-plane of the OMT and the dashed is for the H-plane. For the cross polarization, the solid line is E-plane input, H-plane output and the dashed line is H-plane input, E-plane output. All properties improve at the highest RF frequencies, leading to decreased spurious polarization for channels J1 and J2 relative to J3.

of the feed was measured to be ≤ -40 dB (see figure 5). It is primarily the off-axis response in the near side-lobes that show cross-polarization. As shown in Carretti et al. (2001), the quadrupolar anisotropy on scales comparable to the FWHM is the dominant source of spuriously correlated response by the feed. POLAR's vertical drift scan geometry and low side-lobe level reduced the effect of cross-polarized optical response to negligible levels.

5.3. Non-Ideal Correlation Radiometer Behavior

The most significant non-ideal behavior of the correlation radiometer results from electrical path length mismatch between the input arms. From equation (9) the correlator's DC output is proportional to $\cos(\Delta\phi_\nu)$ where $\Delta\phi_\nu$ is the phase shift between the two arms of the radiometer. A 90° phase shift therefore results in a zero signal-to-noise ratio. The path length difference ΔL introduces a dispersive phase shift, $\Delta\phi(\nu, \Delta L)$. Recalling that POLAR measures the cross-correlation at $\tau = 0$ lag, and assuming constant power spectra across the RF band for the source, beam, and radiometer transfer functions, from equation (9) we have:

$$R(0) \propto \int_{-\pi}^{+\pi} \tilde{\gamma}(\theta) \tilde{B}(\theta) |\tilde{H}|^2 d\theta \int_{\nu_o}^{\nu_o + \Delta\nu_{RF}} \cos \Delta\phi d\nu. \quad (23)$$

The contribution of each spectral component is thus weighted by the cosine of its phase. It is therefore imperative to accurately match the path lengths in the system. To determine the phase mis-match a completely polarized signal is injected into the OMT input. The injected signal is swept in frequency across the RF band. By measuring the frequency modulation of the correlator spectrum by the $\cos \Delta\phi$ envelope, the equivalent path length imbalance can be determined. The path difference measurements agreed with measurements of the physical waveguide path difference. To balance the path lengths, sections of waveguide were added to the shorter arm of the receiver. Comparing the theoretical NET given the RF bandwidth to the measured NET, we estimate that the differential phase shift for the correlation channels was $< 20^\circ$.

The remaining non-ideality results from gain asymmetry between arms, across the band passes. These effects can be caused by mismatched bands, temperature dependence, and phase instability of the amplifiers and/or the correlator. In practice it is impossible to eliminate all such effects. Following Thompson et al. (1998), in table 2 estimates of the tolerable level of a few effects which could contribute to a 2.5% degradation of the signal-to-noise ratio of the correlation receiver.

5.4. Polarimetric Offsets

In the analysis, for each rotation of the polarimeter, the correlator outputs are binned into rotation angle θ_t and fit to

$$I(\theta_t) = I_o + C \cos \theta_t + S \sin \theta_t + Q \cos 2\theta_t + U \sin 2\theta_t. \quad (24)$$

where $\theta_t = 2\pi ft$ and $f = 0.033$ Hz. In addition to the Stokes parameters Q and U , the terms C and S are monitored to determine our sensitivity to rotation-synchronous systematic effects, and to monitor atmospheric fluctuations. Phase sensitive detection at twice the rotation frequency removes I_o and other instrumental effects that are not modulated at this frequency.

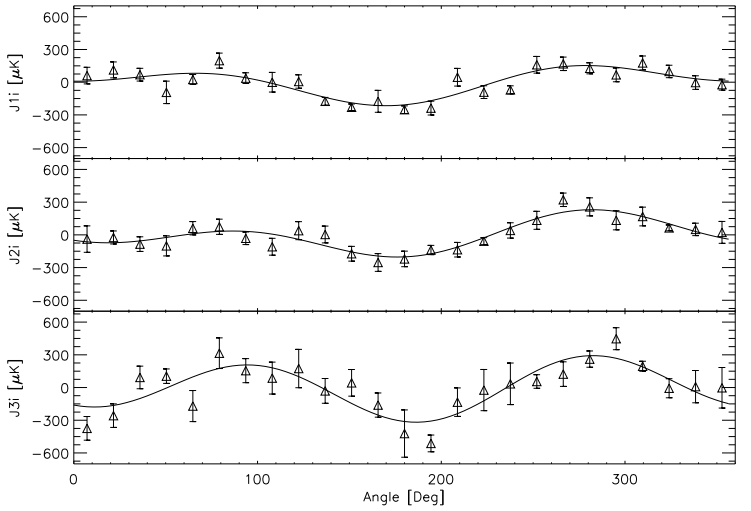


FIG. 13.— Correlator outputs binned into rotation angle for 206 rotations (1 hour 43 minutes) of data obtained during observations on 2 May 2000. The DC offset ($I_o \simeq 100$ mK) of each channel has been removed. Unpolarized offsets and Stokes parameter offsets are visible for each of the three correlator channels. The relative phasing and offset magnitudes are consistent with the model presented in sub-section 5.4. Fits to the Stokes parameter offsets are presented in table 3.

Figure 13 shows the output of 206 co-added rotations (1 hour 43 minutes of data) from the night of 2 May 2000 binned into a single rotation to increase the signal to noise ratio of the systematic effect. Fits to I_o, C, S, Q, U for these plots result in the Stokes parameter offsets for each channel in the instrumental coordinate system.

The cause of the offset was carefully investigated. Initially, the magnetic coupling of the cryogenic isolators to the earth's field was suspected. Helmholtz coils were used to produce a field of $\simeq 10$ Gauss at the position of the isolators. The offsets remained unchanged after one hour of integration with the coils in place. The coils were then located at four other azimuthal positions around the dewar and no observable effects were noticed.

The modulated signals were found to be consistent with a common *optical* offset for each channel (as indicated by the consistent phasing of the signals across the channels). Unpolarized flux is correlated in the receiver due to the OMT's cross polarization and imperfect isolation, causing $I_o \neq 0$. The optical flux is believed to be unpolarized, but anisotropic, with a dipolar and quadrupolar dependence on the rotation angle θ_t , producing spuriously polarized components Q and U . The quadrupole anisotropy is most likely caused by the outer, reflecting, ground screen, which is a square 'scoop' centered on the dewar axis, while the dipole anisotropy is attributed to the feed horn being located $\simeq 3$ inches radially outward from the dewar axis centerline. The dipolar (S and C) and quadrupolar (Q and U) components are present at levels that are 30 dB lower than the unpolarized offset I_o . The frequency dependence of the offset is consistent with the OMT's performance. Both the cross-polarization and the isolation of the OMT degrade with decreasing RF frequency. Therefore, since the radiometer offset is primarily due to the OMT's cross-

polarization, the offset will be largest for J3 since it is the lowest frequency band. Atmospheric emission that is truly polarized by the groundscreen would have a spectrum that increases with frequency, contrary to what was observed.

Table 3 presents the offsets as a function of channel for the 2 May 2000 data. The offset phase angle dependence was roughly constant throughout the season, whereas the magnitudes of the offsets were correlated among channels and varied with observing conditions; most notably humidity and atmospheric opacity. This again supports the hypothesis that unpolarized anisotropic atmospheric flux is polarized by the OMT.

To be used in the cosmological data analysis, the magnitude and phase of the offset must be stable over > 4 hour timescales. Approximately 50% of the surviving sections of data have stable offsets for > 8 hour periods of time. Our sensitivity to Stokes parameter offsets is minimized by constraining the demodulated data to have no dependence on an overall Stokes parameter offset. This is a generalization of the procedure outlined in Bond, Jaffe, & Knox (1998) to treat (unpolarized) offsets for CMB temperature anisotropy experiments. The offset removal procedure not only constrains the final maps produced to have zero offset, but also accounts for the sensitivity degradation induced by the offset removal. The offsets are computed from maps produced for each channel for each contiguous 3 hour block of data that survives the data editing criteria (denoted as a “section”). The offset for each section is determined by enforcing consistency (within the error bars) between the maps constructed from all sections measuring the same pixel on the sky. This induces correlations between sections of data, and between adjacent pixels mapped in the same section. The offset removal and data analysis procedure are discussed in detail in O’Dell (2002b).

6. METEOROLOGICAL EFFECTS AND DATA SELECTION

A variety of weather-related phenomena was encountered during the Spring 2000 observing campaign. We compiled data on the Pine Bluff, Wisconsin area from both the National Weather Service and the GOES-8 satellite data served by the Space Sciences and Engineering Center at the University of Wisconsin-Madison²⁷.

6.1. General Atmospheric Effects

The GOES-8 data are recorded hourly, and measures a $\simeq 5$ km by 5 km area, within 20 km of the POLAR observatory. It provided the cloud cover fraction of the area, and precipitable water vapor (PWV) column height (as well as a host of other weather variables). Periods of high PWV correlated with formation of dew and ice on the vacuum window. Astrophysical data acquired during these periods were not used in the analysis due to the spurious correlation produced by reflection from the dew/ice on the window. Cloud cover fraction exhibits a bimodal histogram, with more than 35% of the time classified as ‘totally clear’ and about 15% of the time categorized as completely overcast. Partially cloudy days account for the other 50% of the distribution. POLAR’s two total power channels monitor the atmospheric zenith temperature. Figure 14 presents a histogram of daily atmospheric zenith temperature measured over the observing season by POLAR.

²⁷ <http://www.ssec.wisc.edu>

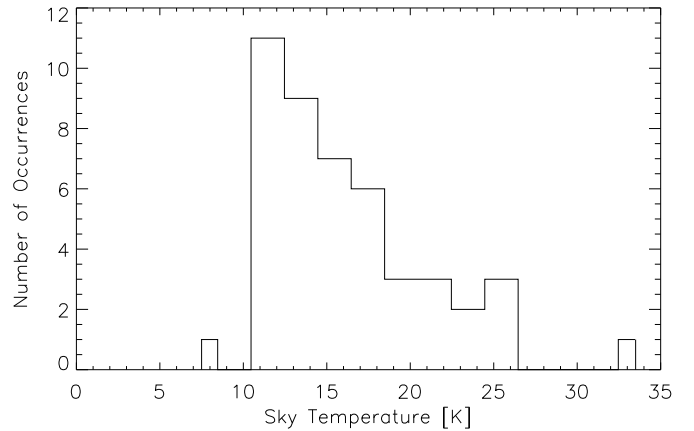


FIG. 14.— Daily atmospheric zenith antenna temperature distribution for the Spring 2000 observing campaign.

6.2. Solar and Lunar Effects

Based on the geometry of the inner, co-rotating, conical groundscreen, some solar radiation will enter this screen when sunlight propagates over the outer (fixed) groundscreen. This happens at a solar elevation of $\simeq 10^\circ$. However, for this light to enter the horn, it must scatter many times off the inner ground screen and will then be absorbed by the inner screen’s Eccosorb coating. Below this elevation of 10° , solar radiation must undergo a double diffraction to enter the system. The amount of sunlight in the beam-pattern steeply increases as the sun rises until the sun’s elevation reaches $\simeq 49^\circ$, at which time radiation from the sun can directly enter the horn. We found that, in practice, solar contamination was undetectable below a solar elevation of 30° . To be conservative, we eliminated all data taken with the sun more than 20° above the horizon. Since data were collected 24 hours per day, this represents a sizeable 38.6% of our data, or $\simeq 288$ hours.

The moon is a bright microwave source, corresponding roughly to a thermodynamic temperature of 220 K. Its emission is dependent upon frequency, lunar phase, and polarization. Using the lunar emission model presented in Keihm (1983), the *COBE* team calculate the lunar emission in both polarization states at 30, 50, 90 GHz, and show that the polarized lunar antenna temperature at 31 GHz is $\lesssim 1$ K (Bennett et al. 1992). Using a variation of this model, and the POLAR beam patterns, we have estimated the polarized antenna temperature of the moon as a function of elevation angle. During the Spring 2000 observing season the highest lunar elevation was 68.4° . We removed all data when the moon was more than 50° in elevation; this corresponds to about 1.2% of the data, and reduces the maximum lunar contribution to be $\ll 1 \mu\text{K}$.

6.3. Atmospheric Data Cut

The primary data quality cut for selecting astrophysical data is based on the statistics of the *S* and *C* terms of fits to equation 24. This cut is referred to as the 1ϕ cut. As previously mentioned, the *S* and *C* components are statistically independent from the *Q* and *U* components. Since the 1ϕ component probes the power spectrum of the radiometer at lower frequencies, it is more susceptible to

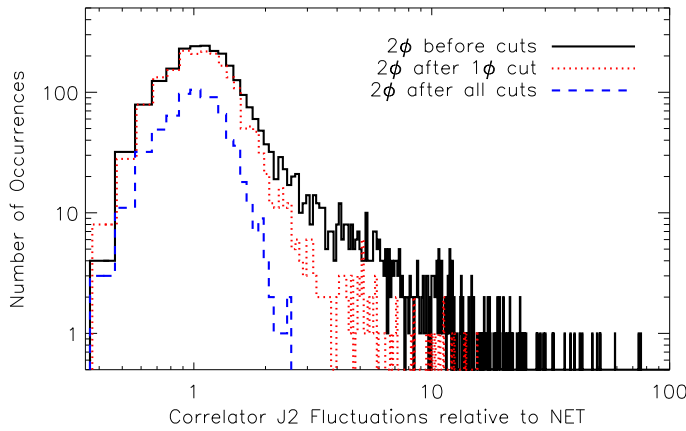


FIG. 15.— Distribution of correlator fluctuations for 7.5 minute averages, as a function of cut level. The solid (black) curve shows the fluctuation level at twice the rotation frequency, relative to the NET of the system, for the in-phase channel J2I, after cuts removing sun, moon, and dew contamination have been applied. The dotted curve shows the same information, but after the 1ϕ cut has been applied. This cut removes a large number of high-level outliers, but much of the remaining data still are contaminated. The dashed curve shows the distribution after all cuts have been applied; very little if any 2ϕ contamination remains.

contamination by atmospheric fluctuations, and can therefore be used as an unbiased probe of data quality which is independent of the astrophysical data. For each 7.5 minute segment of data, the fluctuations in S and C are compared to 1) the expected fluctuation level from gaussian white noise and 2) fluctuations in S and C from the QPC which, as mentioned, display pure white noise power spectral densities with amplitude equal to the radiometer NET. Figure 15 shows the distribution of fluctuations in the 2ϕ component for the 7.5 minute averages for channel J2, for the Spring 2000 observing campaign. Also indicated are the cut levels used in the analysis presented in Keating et al. (2001) and the in-phase channel (IPC) distribution after the 1ϕ cut has been applied.

7. SUMMARY

We have described the design and performance of a novel instrument which was recently used to set upper limits on the polarization of the CMB. The simplicity of the optical design of the polarimeter and the observing strategy resulted in minimal systematic effects. Observations were conducted from a convenient location near the University of Wisconsin – Madison. The site was useful for work at 30 GHz and its proximity afforded us the ability to diagnose problems and make rapid adjustments to optimize instrumental performance while still in the field. While no evidence for CMB polarization was detected with POLAR, the upper limits are impressive given the brief observing season available during Spring 2000. This is attributable to the low noise of the HEMT amplifier front-end and the modest modulation requirements permitted by the stable correlation radiometer back-end. POLAR has proven to be extremely versatile. Starting in January 2001 the POLAR radiometer has been used as the receiver in a search for CMB polarization at small angular scales: COsmic Mi-crowave Polarization at Small Scales (COMPASS). Results

from COMPASS are forthcoming and will further demonstrate the viability of the correlation polarimeter technique.

We are grateful to a number of people who influenced the design and analysis of POLAR. Initial theoretical guidance and encouragement came from Alex Polnarev and Robert Brandenberger. Dick Bond, Robert Crittenden, Angelica de Oliveira-Costa, Wayne Hu, Lloyd Knox, Arthur Kosowsky, Kin-Wang Ng, and Matias Zaldarriaga provided crucial insight during the development and analysis phases, and vastly enhanced the scientific impact of the project. We are also indebted to several experimentalists who worked-on, supported, or guided, the construction of the instrument: Brendan Crill, Khurram Farooqui, Kip Hyatt, Slade Klawikowski, Alan Levy, Phil Lubin, Melvin Phua, Dan Swetz, David Wilkinson, Grant Wilson, Ed Wollack. BGK and CWO were supported by NASA GSRP Fellowships. POLAR’s HEMT amplifiers were provided by John Carlstrom. This work has been supported by NSF grants AST 93-18727, AST 98-02851, and AST 00-71213, and NASA grant NAG5-9194.

REFERENCES

Bennett, C. L., et al. 1992, ApJ, 391, 466
 Bond, J. R., Jaffe, A. H., & Knox, L. 1998, Phys. Rev. D57, 2117
 Brouw, W. N., & Spoelstra, T.A. 1976, A&AS, 26, 129
 Carretti, E., et al. 2001, New Astronomy, 6, 173
 Chandrasekhar, S. 1960, *Radiative Transfer*, Dover, New York
 Cheng, E., et al. 1979, ApJ, 232, L139
 Chu, T. 1975, Bell Sys. Tech. J., 54, 1665
 Clarricoats, P., & Olver, A., 1984 *Corrugated horns for microwave antennas*, Peter Peregrinus
 Davies, R. D., et al. 1996, MNRAS, 278, 883.
 Draine, B. T., & Lazarian, A. 1998, ApJ, 494, L19
 Faris, J., 1966, J. of Results of the NBS, 71C
 Fujimoto, K., 1964, IEEE-MTT , March p. 203
 Gasiewski, A., & Kunkee, D., 1993, IEEE-MTT, 41, 767
 Goldsmith, P. 1998, *Quasioptical Systems*, IEEE Press, New York
 Gunn, J. E., & Peterson, B. A. 1965, ApJ, 142, 1633
 Hu, W., and White, M. 1997, New Astron., 2, 323
 Janssen, M.A.. et al. 1979, IEEE Trans. Antennas and Prop. 27(4), 551
 Johnson, D., & Wilkinson, D. 1987, ApJ, 313, L1
 Jackson, J. D., 1975, *Classical Electrodynamics*, Wiley
 Kamionkowski, M., Kosowsky, A., and Stebbins, A. 1997, Phys. Rev. D, 55, 7368
 Keating, B., Polnarev, A., Steinberger, J., & Timbie, P. 1998, ApJ, 495, 580
 Keating, B., et al., 2001, ApJ, 560, L1
 Keihm, S.J. 1983, Planetary Sci. Inst. Rep., K.
 Kraus, J. 1986 *Radio Astronomy*, McGraw-Hill, New York
 Lubin, P., & Smoot, G. 1981, ApJ, 245, 1 L51
 Mason, B., et al. 1999, AJ, 118, 2908
 Nanos, G. 1979, ApJ, 232, 341
 Netterfield, C.B., et al., 1995, ApJ, 474, L69
 O’Dell, C.W., et al. 2002, IEEE MTT, accepted
 O’Dell, C.W. 2002, Ph.D. Thesis, U. of Wisconsin - Madison, astro-ph/0201224
 Pospiszalski, M. 1992, IEEE MTT-S Digest, 1369
 Pozar, D. 1990, *Microwave Engineering*, New York, Addison-Wesley
 Rohlf, K. 1996, *Tools of Radio Astronomy*,
 Rybicki, G. B., & Lightman, A. 1979, *Radiative Processes in Astrophysics*, New York, Wiley
 Sironi, G. et al. 1997, New Astron., 3, 1
 Tegmark, M. 1997, Phys. Rev. D, 56, 4514
 Tegmark, M., & de Oliveira-Costa, A. 2001, Phys. Rev. D, 64, 63001
 Thompson et al., 1998, *Interferometry and synthesis in radio astronomy*, Krieger, Malabar
 Timbie, P., & Wilkinson, D. 1990, ApJ, 353, 140
 Wang, X., Tegmark, M., & Zaldarriaga, M. 2001, astro-ph/0105091
 Wollack, E.J. 1995, Rev. Sci. Inst. 66, 4305
 Wollack, E.J., and Pospiszalski, M., 1998, IEEE MTT-S Digest, 669

Wollack, E.J., et al., 1997, ApJ, 476, 440
Zaldarriaga, M., & Seljak, U. 1997, Phys. Rev. D, 55,1830
Zaldarriaga, M., Spergel,D., Seljak, U 1997 ApJ,488,1
Zaldarriaga, M. 1997,Phys. Rev. D,55,1822
Zaldarriaga, M. 1998, ApJ, 503, 1
Zhang, X., et al. 1993, IEEE-MTT 41, 8

TABLE 2

TOLERANCES ON CORRELATION POLARIMETER FREQUENCY RESPONSE VARIATIONS FOR A 2.5% REDUCTION IN SIGNAL TO NOISE RATIO (RELATIVE BETWEEN ARMS).

Type of Variation	Permissible Level
Gain Slope	3.5 dB across band
Gain Sinusoidal Ripple	2.9 dB peak-peak
Frequency Band Centroid Offset	5% of $\Delta\nu_{RF}$
Phase Shift Between Bands	12.8°

TABLE 3

POLAR OFFSETS 2 MAY 2000. 206 ROTATIONS (1 HOUR 43 MINUTES OF DATA) CO-ADDED AND BINNED INTO ROTATION ANGLE[†]

Channel ^a	I_o ^b [mK]	C ^c [μ K]	S ^d [μ K]	Q ^e [μ K]	U ^f [μ K]	P ^g [μ K]	ϕ ^h [degrees]
J3I	133.8 ± 1.0	75.4 ± 38.0	-31.7 ± 38.0	-236.3 ± 38.0	-73.6 ± 38.0	247.5 ± 47.6	8.7 ± 4.7
J2I	83.6 ± 1.0	76.2 ± 20.0	-91.3 ± 20.0	-125.8 ± 20.0	-25.9 ± 20.0	128.4 ± 23.6	5.8 ± 4.6
J1I	88.1 ± 1.0	108.3 ± 20.0	-48.4 ± 20.0	-99.3 ± 20.0	21.0 ± 20.0	101.5 ± 23.7	-6.0 ± 5.8
J3Q	15.76 ± 0.09	13.8 ± 38.0	15.0 ± 38.0	8.4 ± 38.0	68.9 ± 38.0	69.5 ± 42.1	41.7 ± 52.5
J2Q	5.57 ± 0.05	-9.6 ± 20.0	-25.3 ± 20.0	29.6 ± 20.0	-28.0 ± 20.0	41.0 ± 28.3	-22.5 ± 22.9
J1Q	7.15 ± 0.04	7.3 ± 20.0	-19.1 ± 20.0	-20.3 ± 20.0	12.7 ± 20.0	23.8 ± 27.7	-16.5 ± 31.5

[†] refer to Fig. 13 for data.

^a 'I' refers to in-phase channels; 'Q' refers to quad-phase channels.

^b Unpolarized, unmodulated, intensity.

^c Dipole modulated cosine term.

^d Dipole modulated sine term.

^e Quadrupole modulated Q term.

^f Quadrupole modulated U term.

^g Magnitude of polarized offset $P = \sqrt{Q^2 + U^2}$. Over the course of the observing season, the offsets were always in the order $P(J3) > P(J2) > P(J1)$.

^h Phase angle of polarized offset $\phi = \frac{1}{2} \tan^{-1} \frac{U}{Q}$. Throughout the season, the phase angles of the offsets were roughly constant for the in-phase channels.